

## Griffiths phase arising from local lattice distortion and spin glass above the Curie temperature in Ni<sub>2</sub>MnSb polycrystalline Heusler alloy

Fanhua Tian<sup>1,\*</sup>, Qizhong Zhao,<sup>1</sup> Jiale Guo,<sup>1</sup> Yin Zhang,<sup>1</sup> Minxia Fang<sup>1</sup>, Tieyan Chang<sup>1,2</sup>,  
Zhiyong Dai,<sup>1</sup> Chao Zhou,<sup>1</sup> Kaiyan Cao,<sup>1</sup> and Sen Yang<sup>1,†</sup>

<sup>1</sup>MOE Key Laboratory for Nonequilibrium Synthesis and Modulation of Condensed Matter, School of Physics,  
Xi'an Jiaotong University, Xi'an 710049, China

<sup>2</sup>NSF's ChemMatCARS, The University of Chicago, Lemont, Illinois 60439, USA



(Received 23 November 2023; accepted 23 May 2024; published 4 June 2024)

In this work, the phenomenon of downward deviations from the Curie-Weiss law is found above the Curie temperature (329–458 K) in Ni<sub>2</sub>MnSb polycrystalline Heusler alloy, and it was confirmed by the change in inverse magnetic susceptibility under different magnetic fields that it is the Griffiths phase. This abnormal phenomenon can be attributed to short-range nanoferrromagnetic clusters caused by local lattice distortion within the paramagnetic state. The ac magnetic susceptibility further showed characteristics of long-range disordered and short-range ordered glassy magnetic states in Griffiths phase range, where the magnetization intensity of the spin glass state has a frequency dependence. This work revealed the nature of the Griffiths phase in Heusler alloys and observed the characteristics of spin glass at high temperatures, providing experimental evidence and support for the study of high-temperature spintronics.

DOI: [10.1103/PhysRevB.109.224405](https://doi.org/10.1103/PhysRevB.109.224405)

### I. INTRODUCTION

The Griffiths phase theory is based on the idea of “local” phase transitions in diluted systems due to the finite probability of randomly large, pure, and differently diluted clusters [1]. The Griffiths model accounts for a magnetic system in which magnetic interactions are given by disorder sets, and random distribution of these interactions should be in such a mood where different values for the exchange constant can be assigned to the different sites of the lattice in a random way [2–5]. In this framework, the Griffiths phase is a peculiar state that is predicted to occur in randomly diluted Ising ferromagnetic (FM) systems, in which the magnetization fails to become an analytic function of the magnetic field over a temperature range  $T_C < T < T_G$ . Here,  $T_G$  is the temperature for the onset of completely random magnetic interactions and  $T_C$  is the temperature for the appearance of spontaneous magnetization. Experimentally, the Griffiths phase is signed by anomalies in magnetic susceptibility, specific heat, transport properties, and the nonlinearity variation of inverse magnetic susceptibility in the nominal paramagnetic (PM) phase [6–8].

Since the concept of the Griffiths phase was proposed, it is mainly found in the rare-earth intermetallic system  $R_5(\text{Si}_x\text{Ge}_{1-x})_4$  ( $R$  = rare earth) and perovskite manganites  $R_{1-x}A_x\text{MnO}_3$  ( $R$  = rare-earth ions and  $A$  = divalent ions) [9–13]. The origin of the Griffiths phase varies for different materials. In rare-earth intermetallic systems, the Griffiths phase arises due to the percolative nature of the distribution

of short-range FM clusters in a magnetic disordered, apparently PM regime [9,10,14]. In contrast to this, the Griffiths phase in the perovskite manganites is supposed to originate from the random distribution of exchange interaction strength [12,13,15]. After in-depth research, the giant magnetoresistance effect in perovskite materials and the giant magnetocaloric effect of rare-earth intermetallic systems may be related to the Griffiths phase. In recent research, the Griffiths phase has also been discovered in Heusler alloys [16–18]. However, there is still a lack of in-depth research and evidence on its origin.

Heusler alloys were identified as a special group of magnetic materials, originally composed of nonmagnetic elements, exhibiting ferromagnetism in nonmagnetic element compounds [16]. The general stoichiometric formula of full-Heusler alloys is  $X_2YZ$ , where  $X$  and  $Y$  are transition metals and  $Z$  is either a metal or a semimetal. In these alloys, differences in  $p$ - $d$  orbital hybridization between the main group and transition metal atoms lead to differences in atomic site occupation [19], lattice parameters [20], magnetism [21], and phase stability [22]. In previous research, Heusler alloys would experience the magnetic and structural phase transitions that the phase of PM austenite  $\rightarrow$  FM austenite  $\rightarrow$  FM/antiferromagnetic martensite  $\rightarrow$  FM martensite  $\rightarrow$  the low-temperature spin-glass (SG) state during the process from high to low temperatures [19–22]. Based on this, many interesting properties are induced: magnetocaloric effect [23,24], shape memory effect [25,26], exchange bias effect [27,28], and magnetoresistive effect [29,30]. Therefore, the study of magnetic states is the basis for the study of magnetic materials, and understanding the causes of magnetic states is crucial to the study of materials. However, so far, there are still the following questions in understanding magnetic inhomogeneity above  $T_C$  in Heusler alloys: (1) How is Griffiths

\*Corresponding author: [tfh2017@xjtu.edu.cn](mailto:tfh2017@xjtu.edu.cn)

†Corresponding author: [yangsen@xjtu.edu.cn](mailto:yangsen@xjtu.edu.cn)

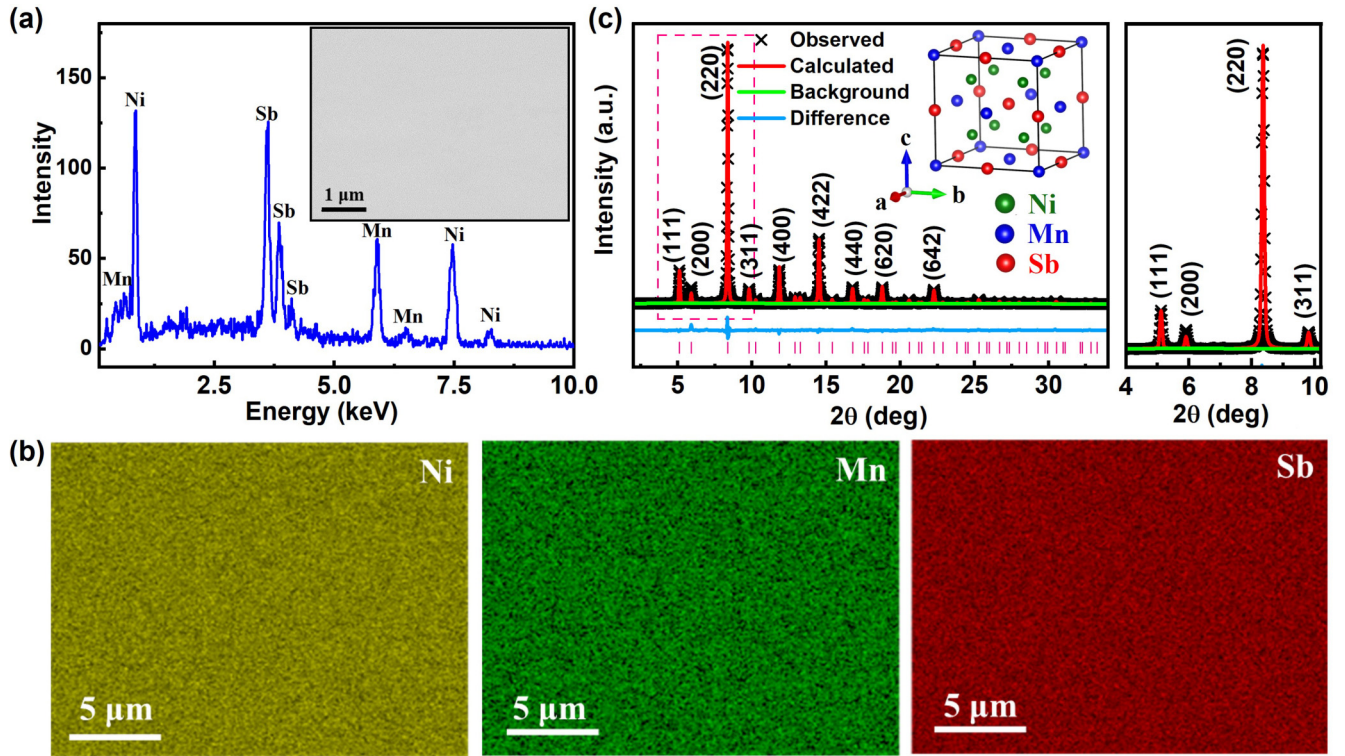


FIG. 1. (a) EDS analyzed the element ratio of alloy. The element ratio is calculated by the software that comes with the instrument according to the intensity ratio to standard samples. Inset: Backscattered electron testing of alloy. (b) EDS mapping for the SEM image [inset Fig. 1(a)]; the corresponding elemental mapping images of the Ni, Mn, and Sb, atoms, respectively. (c) The high-resolution XRD spectra of the  $\text{Ni}_2\text{MnSb}$  alloy were measured at room temperature; the partial enlarged view is shown in the right of (c), and the  $L2_1$  structure is illustrated in the inset.

phase in Heusler alloys generated? (2) What is its microscopic magnetic state? (3) Has the structure changed?

In this paper, the Griffiths phase and its causes in  $\text{Ni}_2\text{MnSb}$  Heusler alloys are studied. It is found that the Griffiths phase appears in the range of the temperature 329–458 K above  $T_C$ . Research on ac magnetic susceptibility exhibits the short-range glassy magnetic state of the Griffiths phase. Further analysis shows that this Griffiths phase stems from local lattice distortion. Our work reveals the nature of the Griffiths phase in Heusler alloys and promotes research on SG.

## II. EXPERIMENTAL DETAILS

The ingot of  $\text{Ni}_2\text{MnSb}$  alloy was prepared by arc melting with high-purity (99.99%) Ni, Mn, and Sb in an argon atmosphere. To ensure high composition homogeneity, the sample was wrapped in the silica tube and then annealed in a vacuum at 1173 K for 24 h. A field-emission scanning electron microscope (SEM; JEOL JSM-7000F, Japan) and transmission electron microscopy (TEM; JEOL JEM-2100, Japan) were used to observe the micromorphology and microstructure of the alloy. Electron energy disperse spectroscopy (EDS) and backscattered electrons were used to observe the element composition and content of the alloy. The alloy was sealed in Kapton capillaries for high-resolution x-ray diffraction (HR-XRD) measurements with  $\lambda = 0.4142 \text{ \AA}$  at beamline 11-BM-B at the Advanced Photon Source, Argonne National Laboratory. The measurements

of magnetic properties, including magnetization-temperature ( $M$ - $T$ ) curves, initial magnetization curves, and ac susceptibility ( $\chi$ ) as a function of temperature were performed by using a superconducting quantum interference device magnetometer (Quantum Design, MPMS-XL-5).

## III. RESULTS AND DISCUSSIONS

As shown in Fig. 1(a), the specific element composition and content are performed and analyzed by EDS. It is seen that the atomic percentage (at. %) of Ni, Mn, and Sb is 49.56, 25.33, and 25.11, respectively. It deviates from the nominal composition ( $\text{Ni} : \text{Mn} : \text{Sb} = 2 : 1 : 1$ ) at an acceptable level, suggesting the reliability of the experiments as well as the high quality of the prepared sample. The single-phase nature has been confirmed by backscattered electrons, as shown in the inset of Fig. 1(a). The microstructure of  $\text{Ni}_2\text{MnSb}$  is chemically homogeneous, and no microchemical segregation is identified. There is no secondary phase formation in the alloy during solidification. In addition, EDS mapping analysis is carried out in Fig. 1(b). The bright spots in different colors correspond to Ni, Mn, and Sb, respectively. The results show that all elements were distributed uniformly throughout the area, consistent with the results of backscattering, and there is no component segregation. The HR-XRD pattern of the  $\text{Ni}_2\text{MnSb}$  polycrystalline alloy is analyzed at room temperature, as shown in Fig. 1(c). The calculated results are based on the cubic structure with space group  $Fm\bar{3}m$ , and the Rietveld

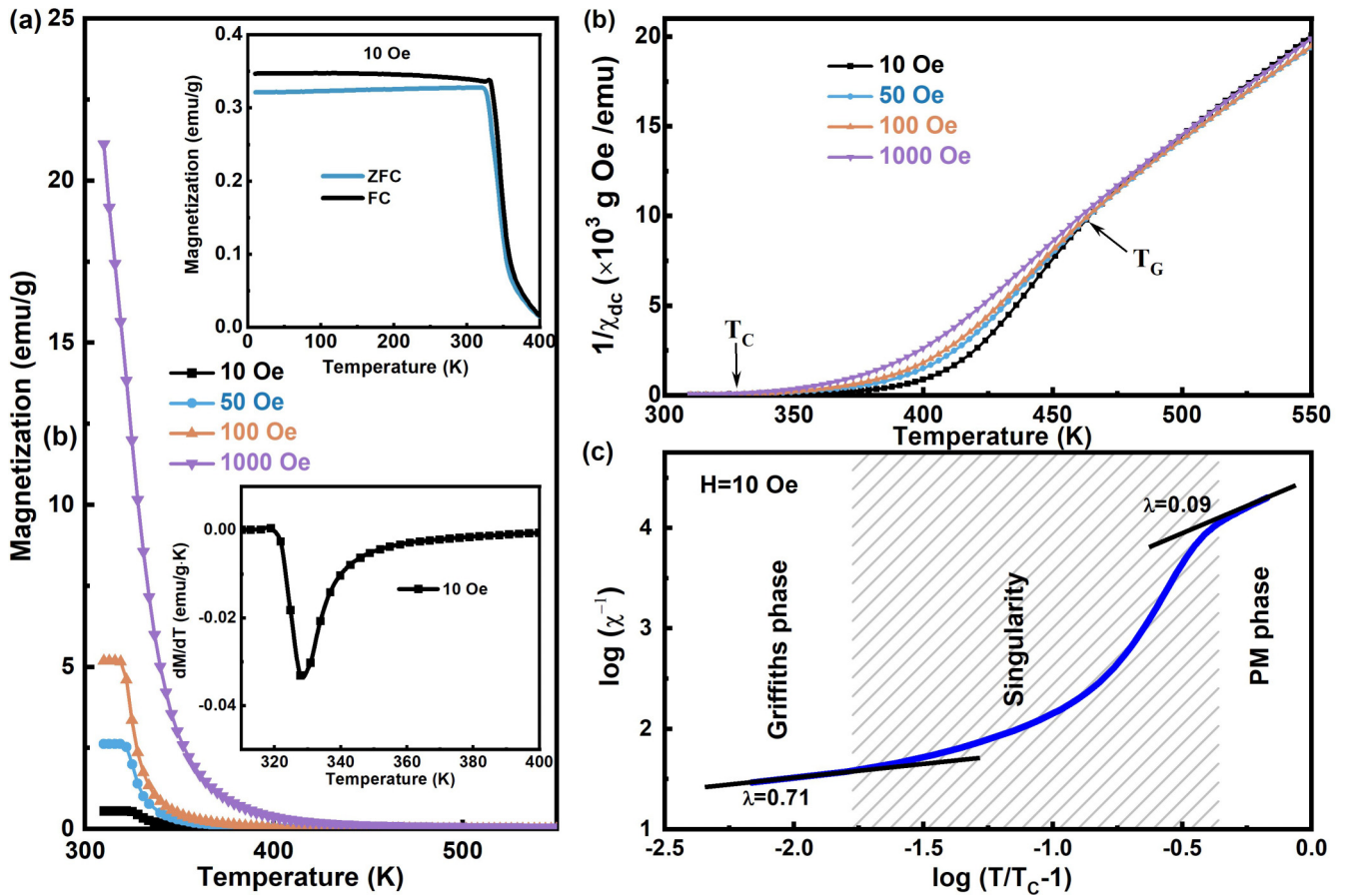


FIG. 2. (a) Field-cooled warming magnetization of  $\text{Ni}_2\text{MnSb}$  measured under different magnetic fields. Inset: (Top) Magnetization as a function of temperature for  $\text{Ni}_2\text{MnSb}$  measured at a low magnetic field of 10 Oe under the ZFC and FC processes. (Bottom)  $dM/dT$  curves for  $\text{Ni}_2\text{MnSb}$  measured at a low magnetic field of 10 Oe. (b) Temperature dependence of inverse susceptibility  $\chi^{-1}$  under different fields for  $\text{Ni}_2\text{MnSb}$ . (c)  $\log_{10} \chi^{-1}$  vs  $\log_{10} (T/T_C - 1)$  plots for the  $\text{Ni}_2\text{MnSb}$  alloy. Black lines are the fitting for data using Eq. (1).

refinements show a good agreement between the experimental and calculated diffraction patterns of the sample, which can be indicated by the small values of the reliability factors ( $R_p = 6.56\%$  profile factor,  $R_{wp} = 7.32\%$  weighted profile factor,  $\chi^2 = 1.12$  goodness of fit) of the Rietveld refinements. The superlattice diffraction peaks (111) and (200) are clearly observed, which indicates that the alloy has an ordered  $L2_1$  structure [31,32]. In the  $\text{Ni}_2\text{MnSb}$  stoichiometric compound, the Ni, Mn, and Sb atoms occupy sublattices, as shown in the inset of Fig. 1(c).

The  $M$ - $T$  curves during the zero field-cooled (ZFC) and field-cooled (FC) processes for  $\text{Ni}_2\text{MnSb}$  alloy under an extra magnetic field of 10 Oe are shown in the inset of Fig. 2(a); the temperature range is 10–400 K. A sharp magnetization change occurred around 329 K, which is  $T_C$ . The  $T_C$  (329 K) is defined as the temperature at which a minimum in the  $dM/dT$  curve recorded at  $H_{FC} = 10$  Oe appears as shown in the bottom of the inset of Fig. 2(a). As the temperature decreases, the magnetization intensity does not obviously change below  $T_C$ . Unlike the canonical Curie phase transition [33,34], the Curie phase transition of  $\text{Ni}_2\text{MnSb}$  lasts close to  $\sim 80$  K. As shown in Fig. 2(a), the  $M$ - $T$  curves were depicted during the FC process under different magnetic fields ( $H_{FC} = 10, 50, 100,$  and  $1000$  Oe). Usually, the presence of ferromagnetism within the PM matrix in the Griffiths phase has been

demonstrated by macroscopic magnetic measurements. The inverse susceptibility  $\chi^{-1}$  as a function of temperature should have a downturn above  $T_C$ , which is considered to be a hallmark of Griffiths singularity and would disappear when the external magnetic field becomes large enough [10,14]. In Fig. 2(b), we have shown the inverse dc susceptibility  $\chi^{-1} = H/M$  versus temperature plots for  $\text{Ni}_2\text{MnSb}$ . In the conventional PM regime (above 458 K), it is obvious that the value of  $\chi^{-1}$  is linearly related to the temperature, which obeys the Curie-Weiss (CW) law. And below a characteristic temperature  $T_G$ ,  $\chi^{-1}$  displays a downward deviation from the CW law and a positive curvature accompanying the region  $T_C < T < T_G$ . The sharp decrease of  $\chi^{-1}$  below  $T_G$  indicates the onset of short-range FM correlation well above  $T_C$ , which is considered a hallmark of Griffiths singularity. On further increasing the magnetic field, the contribution from the PM matrix becomes significant. And at last, when the field is larger than 1000 Oe,  $\chi^{-1}(T)$  is almost linear above  $T_C$ . A similar downward deviation in  $\chi^{-1}(T)$  from the CW law has been observed in rare-earth intermetallic and transition metal oxides [9,13,15], and all those phenomena have been attributed to the formation of the Griffiths phase.

It has been demonstrated in perovskite manganites and other systems that the Griffiths phase can be qualitatively

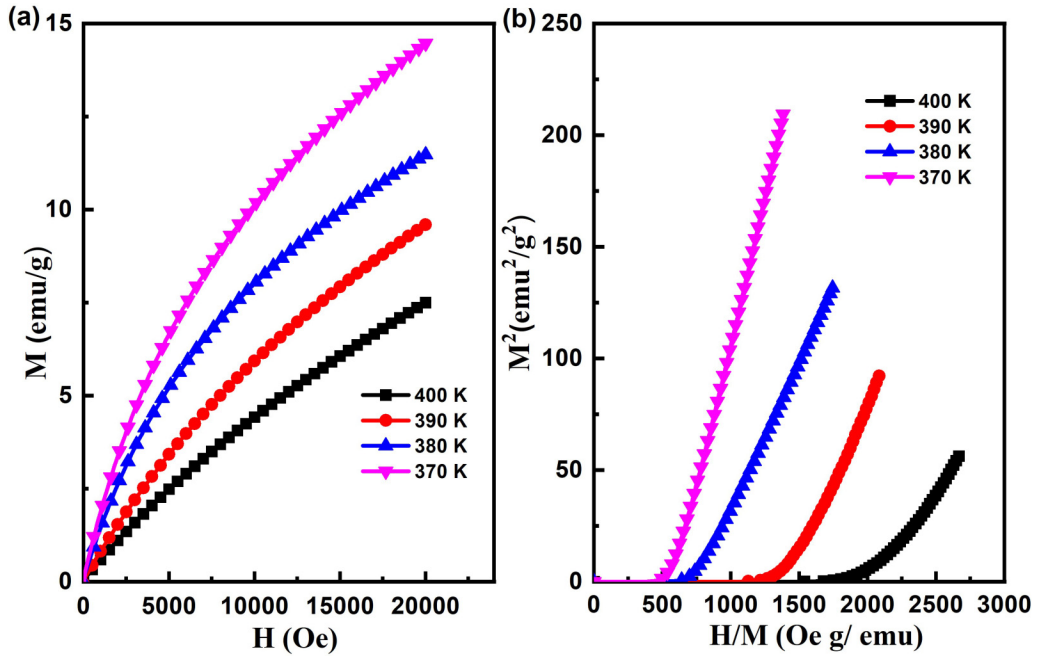


FIG. 3. (a) Isothermal magnetizations for the Ni<sub>2</sub>MnSb alloy at  $T_C < T < T_G$ . (b) Arrott plot of isotherms at  $T_C < T < T_G$ .

studied using the magnetic susceptibility  $\chi^{-1}(T)$  related power-law behavior with the form [14,16]

$$\chi^{-1} \propto (T - T_C)^{1-\lambda}, \quad 0 \leq \lambda \leq 1. \quad (1)$$

To find out the value of  $\lambda$  in both the FM and PM regimes, the  $\chi^{-1} \propto T/T - T_C$  curve in the  $\log_{10}$ - $\log_{10}$  scale was plotted in Fig. 2(c). The slope of the fitted straight lines in both the Griffiths phase regime and the PM matrix gives the values of  $\lambda_G$  and  $\lambda_{PM}$ , respectively. We refined it in the Griffiths phase area ( $330 \text{ K} < T < 458 \text{ K}$ ,  $\lambda_G \approx 0.71 \pm 0.04$  at 10 Oe) and in the conventional PM phase ( $T > 458 \text{ K}$ ,  $\lambda_{PM} \approx 0.09 \pm 0.002$  at 10 Oe). Both values correspond to the previous research where  $0 < \lambda < 1$  for Griffiths phases and close to zero for PM phases [11,14]. At a high field, the values of the exponent remain far from zero value, e.g.,  $\lambda_G \approx 0.19 \pm 0.03$  at 1000 Oe, so the Griffiths-like state remains at 1000 Oe field but shows a weaker downturn. Thus, the magnetic-field suppression of the anomaly displayed by  $\chi^{-1}$  should be explained in terms of masking the FM signal by raising the PM background. Unlike the critical exponents of the conventional FM-PM transition,  $\lambda_G$  is a nonuniversal exponent. The large value of  $\lambda_G$  indicates an apparent Griffiths phase appeared in the Ni<sub>2</sub>MnSb alloy. In addition,  $\lambda_{PM}$  is very small, meaning there will be no Griffiths phase above 458 K, and will be a pure PM phase.

As seen in Fig. 3(a), the initial magnetization curves have been measured in the region  $T_C < T < T_G$ . The initial magnetization curves are not absolutely linear but show perceivable inflection; the contribution to magnetism from FM clusters does not get masked by the PM matrix, indicating the existence of FM character [Fig. 3(a)] [35,36]. This gives further evidence that the Griffiths phase exists above the  $T_C$  in Ni<sub>2</sub>MnSb. To reveal the underlying physics of the Griffiths phase, it is usual to analyze the nature of this magnetic phase

transition in the ambient condition as well as in the presence of an external magnetic field. One approach is to examine the Arrott plots ( $H/M$  versus  $M^2$ ), which can be deduced from the thermodynamic potential with Landau-type expansion near the  $T_C$  as follows [37,38]:

$$G(T, M) = G_0 + AM^2 + BM^4 + \dots - MH, \quad (2)$$

where  $A$  and  $B$  are the Landau coefficients dependent on the temperature. By setting  $\frac{\partial G}{\partial M} = 0$ , the Arrott plots can be described as

$$M^2 = \frac{1}{4B} \frac{H}{M} - \frac{A}{2B}. \quad (3)$$

According to Banerjee's criterion, the material follows first-order phase transition behavior if any curves in Arrott plots show a negative slope. In contrast, its magnetic phase transition is a second-order phase transition on the condition that the slope is positive for all curves in Arrott plots. Based on the initial magnetization curves in Fig. 3(a), Arrott plots are given in Fig. 3(b). The positive slope of all  $H/M$  vs  $M^2$  curves in Fig. 3(b) indicates that the type of magnetic phase transition for Ni<sub>2</sub>MnSb is second order in the region of the Griffiths phase; this also demonstrates that the Griffiths phase is not caused by structural transformations.

In order to investigate the microstructure of Ni<sub>2</sub>MnSb, TEM analysis at 350 K is performed, as shown in Fig. 4. The alloy shows the highly ordered  $L2_1$  structure [Fig. 4(a)] [39], which agrees with the result of the XRD. High-resolution TEM (HRTEM) was also performed to study the details of the microstructure. Figure 4(b) shows a typical HRTEM image of a locally distorted region. The corresponding fast Fourier transformation (FFT) image is shown in Fig. 4(c). The micrograph shows an ordered  $L2_1$  phase, while parts of the electron diffraction pattern can be observed to be characterized by diffuse scattering and additional reflections. This suggests that

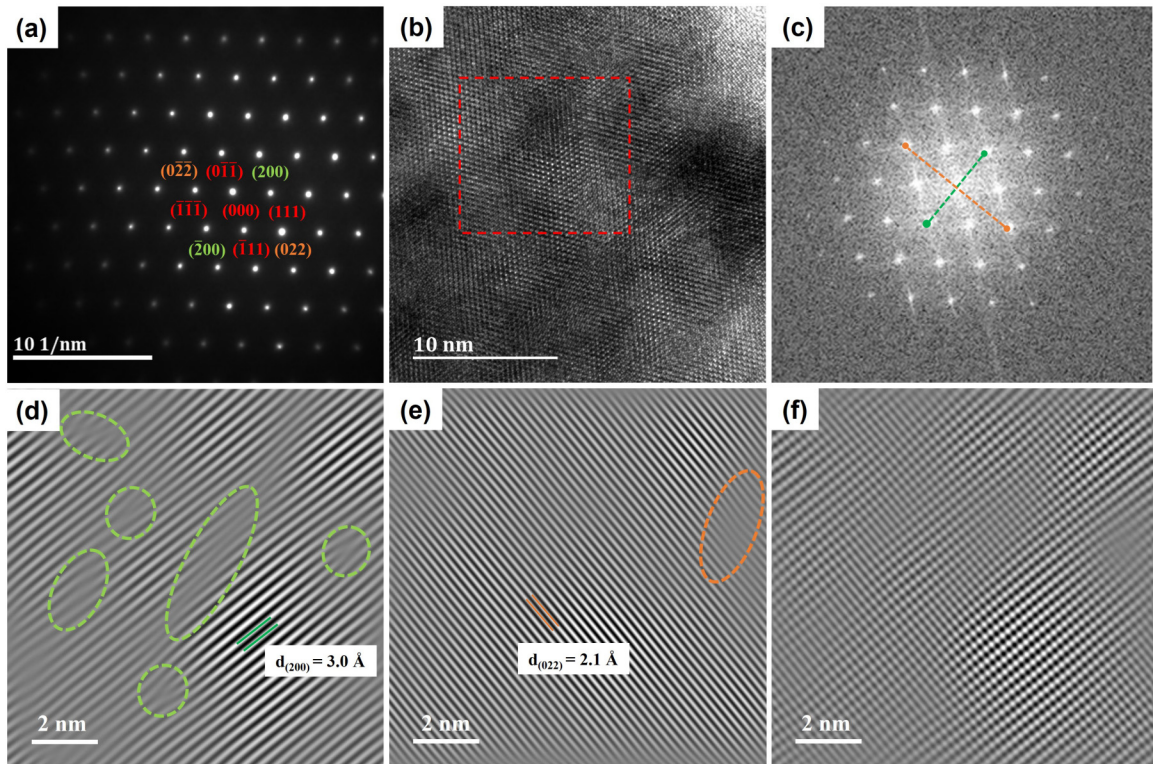


FIG. 4. TEM characterizations of the  $\text{Ni}_2\text{MnSb}$  alloy at 350 K. (a) SAED pattern, (b) HRTEM image, (c) the corresponding FFT pattern extracted from the square marked region, and the corresponding IFFT images obtained by circling fundamental reflections. (d) Two (200) spots and (e) two (022) spots marked in (c) to reveal the modulation waves. (f) IFFT image filtered using all four spots.

there may be slight local lattice distortion. Further inverse fast Fourier transformation (IFFT) was made by selecting the two (002) and (022) fundamental reflections to evaluate the local lattice distortion, as shown in Figs. 4(d) and 4(e), from which the distorted regions can be seen more clearly, e.g., in the green and orange circles regions of Figs. 4(d) and 4(e) [40,41]. In the undistorted region, the measured lattice spacing is  $\sim 3$  Å for (200) and  $\sim 2.1$  Å for (022). Simple superposition of Figs. 4(d) and 4(e) can produce the image Fig. 4(f), which presents a similar pattern as the experimental HRTEM image Fig. 4(b). It is further clearly shown that there is partial local lattice distortion in the ordered  $L2_1$  phase. Because the existence of local lattice distortion leads to the appearance of nano-FM clusters in the PM matrix [42,43], a Griffiths phase appears above the  $T_C$ .

Figure 5(a) shows the temperature dependence of the ZFC and FC magnetization curves. The sample was cooled from 600 to 350 K, which belongs to the Griffiths phase (much higher than  $T_C = 328$  K) under the conditions of ZFC and FC, and the external field was 10 Oe. It can be observed from the FC curve that the sample showed noticeable magnetization response changes in the test temperature range. Its magnetization intensity is  $0.09 \text{ emu g}^{-1}$  at 350 K, which differs from the traditional zero response under a small magnetic field (10 Oe) of the paramagnetic region above  $T_C$ . As the temperature decreases, a clear separation between the ZFC and FC curves is observed, indicating the coexistence of magnetic inhomogeneous phases. To further understand the magnetic state of  $T_C < T < T_G$ , the ac susceptibility with frequency variation is shown in Figs. 5(b) and 5(c). The temperature

dependence of the real part ( $\chi'$ ) and imaginary part ( $\chi''$ ) of the ac were measured at frequencies 1, 3, 33, 133, and 533 Hz, at a probing field of 2 Oe with temperatures from 310 to 550 K. The peaks are pretty broad in the case of  $\chi'$  and sharp in the case of  $\chi''$ . From the ac susceptibility  $\chi'$ , two transitions are clearly observed. A sharp drop in  $\chi'$  is observed around 330 K, which is the  $T_C$  and is very close to the value in Fig. 2(a). In addition, we also observed another unusual transition around 385 K [the enlarged region in the inset of Fig. 5(b)]. The peak shifts towards higher temperature and its value decreases with frequency increasing. This is an essential feature of the SG [44,45]. We used the Vogel-Fulcher relationship to study this SG behavior as follows [44,45]:

$$\omega = \omega_0 \exp \left[ -\frac{E_a}{k_B(T_f - T_0)} \right]. \quad (4)$$

In this expression,  $\omega$  is the angular frequency,  $\omega_0$  is the characteristic frequency of the SG,  $E_a$  is the activation energy of the SG,  $k_B$  is the Boltzmann parameter,  $T_f$  is the freezing temperature, and  $T_0$  is the Vogel-Fulcher temperature, describing the interaction among SG clusters. The ideal freezing temperature  $T_0$  yields 372.6 K by fitting the frequency-dependent modulus dip temperatures with the Vogel-Fulcher relationship [shown in Fig. 5(d)]. Notably, the temperature dependence of magnetization shows a ferromagnetic transition at the  $T_C$  of 329 K, much lower than its ideal freezing temperature  $T_0$ . This demonstrates that the long-range disordered and short-range ordered SG exist from 329 to 385 K.

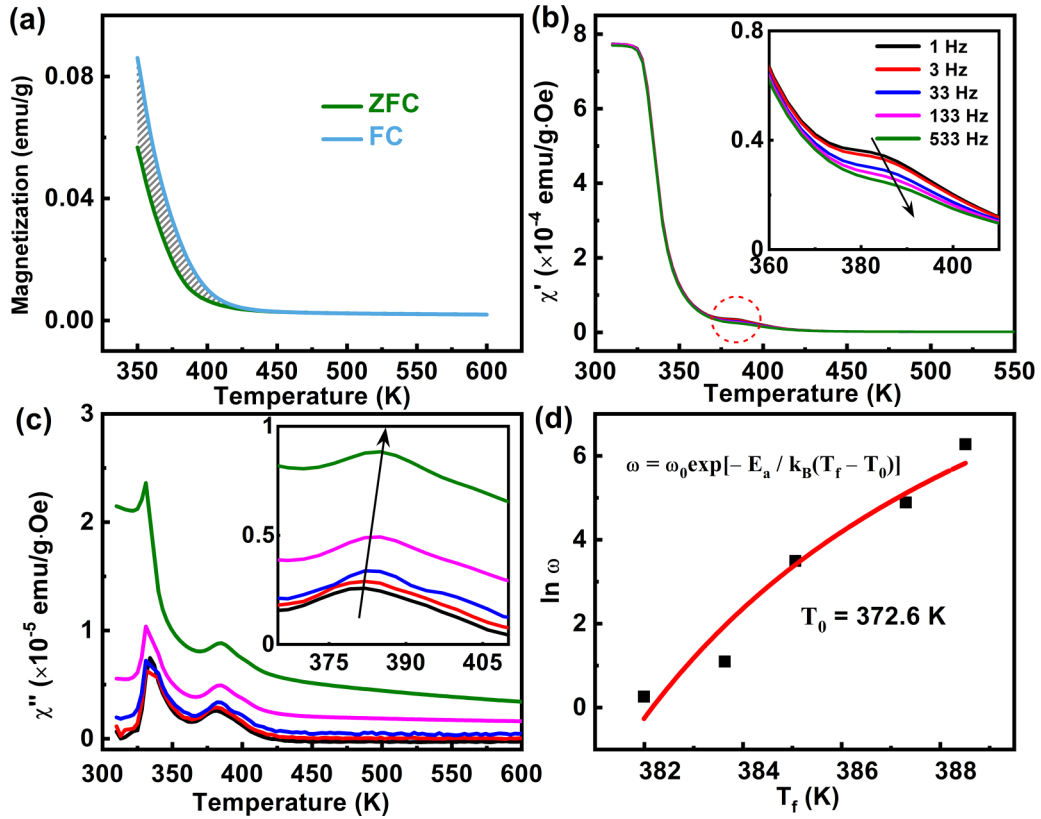


FIG. 5. (a) The temperature dependence of magnetization ( $M$ - $T$ ) curves measured under 200 Oe with the sequences of ZFC and FC. (b), (c) Temperature dependence of the real part and imaginary part of an ac susceptibility measured at different frequencies under an ac field of 2 Oe. In the enlarged part in the insets of (b) and (c), the arrows indicate the direction of high frequencies. (d) Correlation between angular frequency and  $T_f$ . The frequency ( $\omega$ ) dispersion behavior of  $T_f$  conforms to the Vogel-Fulcher relationship.

To further investigate the glassy magnetic state, the magnetic relaxation-time dynamics of the material at different temperatures below  $T_f$  were studied. The time-dependent magnetization has been measured at 350, 360, and 370 K, as shown in Fig. 6(a). The sample has been cooled from 650 to 350, 360, and 370 K in a zero magnetic field for this measurement. After reaching the test temperature and waiting for 1200 s, a 50-Oe magnetic field was applied, and

then the magnetization was recorded as a function of time for  $1.0 \times 10^4$  s. It can be clearly seen that the magnetization data of the sample was analyzed using the stretched exponential function of the form [46,47]

$$M(t) = M_0 - M_r \exp[-(t/\tau_{dc})^\beta], \quad (5)$$

where  $M_0$  is an intrinsic FM component,  $M_r$  is the initial magnetization of the glassy component,  $\tau_{dc}$  is the time

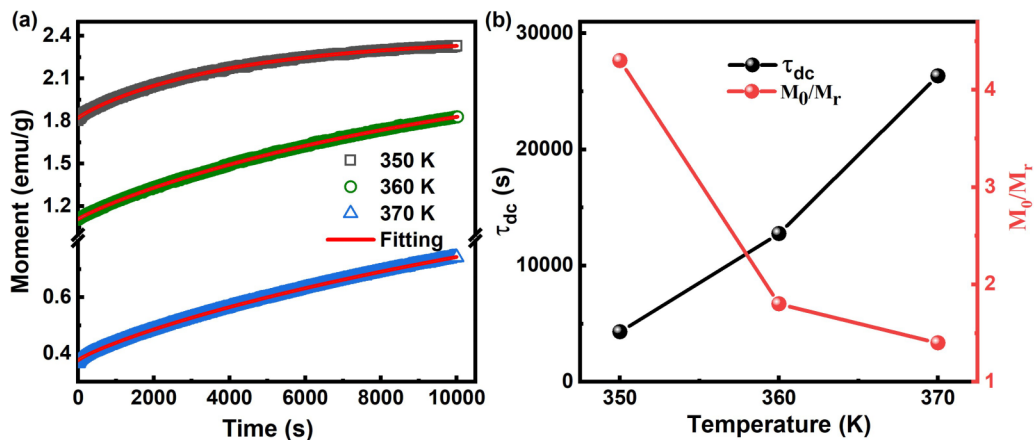


FIG. 6. (a) The time dependence magnetization,  $M(t)$  with a 50-Oe dc magnetic field at 350, 360, and 370 K. The red solid lines exhibit the fit by stretched exponential relation. (b) The change of  $\tau_{dc}$  and  $M_0/M_r$  with temperature.

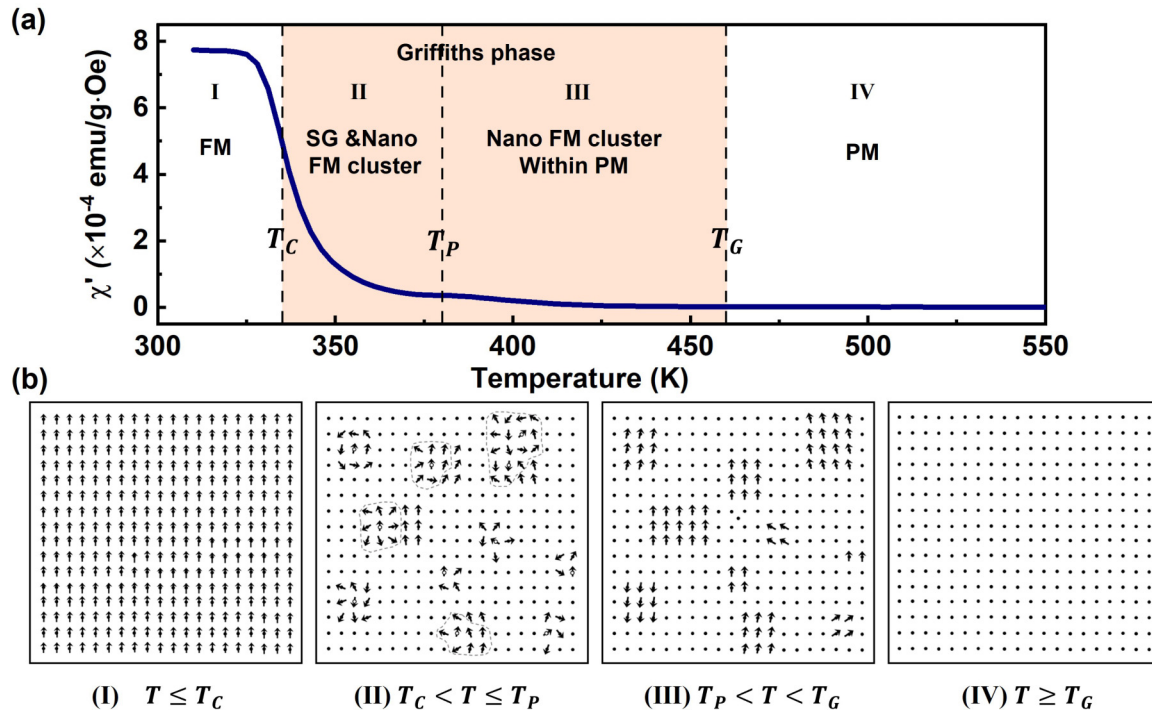


FIG. 7. (a) The transition temperature of the magnetic state of  $\text{Ni}_2\text{MnSb}$  dependent on temperature. (b) Simplified schematic diagrams of the evolution of the magnetic behavior from PM to nano-FM and SG then to FM, as a function of temperature. (I) FM, (II) SG and nano-FM, (III) nano-FM, and (IV) PM. PM is represented by black spots, spins are represented by arrows, and frustrated sites are represented by open circles. The yellow region is the Griffiths phase.

constant, and  $\beta$  (0–1) is related to the relaxation rate. In this relation,  $\beta = 0$  implies that  $M(t)$  is constant, i.e., no relaxation at all, and  $\beta = 1$  implies that the system relaxes with a single time constant. The parameters of  $M_0$ ,  $M_r$ ,  $\tau_{dc}$ , and  $\beta$  were obtained from the best fit to  $M(t)$  data. All  $\beta$  are between 1 and 0, indicating that the material has the characteristics of a SG at the test temperatures. As shown in Fig. 6(b), all the  $\tau_{dc}$ 's are larger than  $1 \times 10^3$ . This is a signature of the nonequilibrium nature of the SG state. The nonzero values of  $M_0$  clearly signify the coexistence of FM/SG components in the relaxation process [46,47]. It is worth noting that  $\tau_{dc}$  decreases and  $M_0/M_r$  increases as the temperature decreases. This indicates that the temperature region closer to the  $T_C$  has more FM parts.

According to the results of  $M$ - $T$ , ac, and magnetic relaxation time, the transition temperatures of the magnetic state of  $\text{Ni}_2\text{MnSb}$  alloy change with temperature as marked in Fig. 7(a).  $\text{Ni}_2\text{MnSb}$  alloy is a typical PM state when the temperature is higher than 460 K. As the temperature decreases, obvious FM signals appear on the PM matrix. As the temperature further decreases, it exhibits the characteristics of SG. Finally, when the temperature is lower than  $T_C$ , it enters the long-range ordered FM state. The simplified schematic diagrams of the magnetic states depending on the temperature are represented in Fig. 7(b). When the temperatures are above  $T_C$ , thermal motion destroys the interaction and each magnetic moment is still free to rotate, basically showing a PM state [see Fig. 7(bIV)]. For  $T_f \leq T \leq T_G$ , corresponding to Fig. 7(bIII), nano-FM clusters appear caused

by the local lattice distortion. As the temperature decreases to  $T_f$ , part of the spin is frustrated, and the surrounding spins also change accordingly. The interaction gradually becomes larger than the thermal motion, and the magnetic moments begin to rotate unfreely, and finally tend to their respective preferred directions, that is, “frozen.” The magnetic freezing direction depends on the resultant force exerted on it by all the surrounding magnetic moments, and because the environment around each magnetic moment cannot be the same, its freezing direction is disordered [Fig. 7(bII)] [48,49]. As the temperature further decreases, all spins are parallel, and the magnetic moment orientation is orderly and does not change with time. There is a long-range FM below  $T_C$ , as shown in Fig. 7(bI).

Generally, traditional SG typically appears at low temperatures ( $< 150$  K) [44–47]. It is worth mentioning that the SG due to the existence of local lattice distortion appears above the  $T_C$  (330–385 K). There are ways to enhance local lattice distortion: (1) Doping other elements into the alloy in small amounts. Since the atomic size of the added element is different from the size of the atoms that make up the materials, local lattice distortion will be enhanced [50]. (2) Most of the materials are polycrystalline, so there will be grain boundaries, and grain boundaries are where local lattice distortion occurs. Obviously, the finer the grains, the more grain boundaries and the more local lattice distortion. Therefore, the alloy structure and properties can be adjusted by preparing the alloy through rapid melt quenching [27]. This kind of SG behavior above the  $T_C$  due to local lattice distortion is also expected to be

discovered in other systems (Fe-Al alloys,  $\text{La}_{1-x}\text{Sr}_x\text{MnO}_3$ , etc.).

#### IV. CONCLUSIONS

In summary, the Griffiths phase behavior having FM spin correlation above the FM transition temperature has been observed in  $\text{Ni}_2\text{MnSb}$  Heusler alloy. The nano-FM clusters exist within the PM matrix in the  $329\text{ K} < T < 458\text{ K}$  temperature range. It can be observed from the relationship between the inverse dc susceptibility  $\chi^{-1}$  and temperature that the Griffiths phase is relatively sensitive to magnetic fields, as the external field increases, this phenomenon will gradually weaken until it disappears. The results of ac magnetization show that the Griffiths phase has the characteristics of a long-range disordered and short-range ordered SG. Further analysis of microstructure suggests that local lattice distortions are responsible for this Griffiths phase. This work reveals the origin of the Griffiths phase in Heusler alloys and provides an in-depth analysis of its magnetic properties. It will

promote further development and practical application of Heusler alloys.

#### ACKNOWLEDGMENTS

This work was financially supported by the National Key Research and Development Program of China (2022YFE0109500), the National Natural Science Foundation of China (Grant No. 51601140), Key Scientific and Technological Innovation Team of Shaanxi Province (2020TD001), and Innovation Capability Support Program of Shaanxi (Grants No. 2018PT-28 and No. 2017KTPT-04). NSF's ChemMatCARS is supported by the Divisions of Chemistry (CHE) and Materials Research (DMR), National Science Foundation, under NSF/CHE-1834750. Use of the Advanced Photon Source, an Office of Science User Facility operated for the U.S. Department of Energy (DOE) Office of Science by Argonne National Laboratory, was supported by U.S. DOE under Contract No. DE-AC02-06CH11357.

- 
- [1] R. B. Griffiths, Nonanalytic behavior above the critical point in a random Ising ferromagnet, *Phys. Rev. Lett.* **23**, 17 (1969).
- [2] A. J. Bray, Nature of the Griffiths phase, *Phys. Rev. Lett.* **59**, 586 (1987).
- [3] R. Shankar and G. Murthy, Nearest-neighbor frustrated random-bond model in  $d = 2$ : Some exact results, *Phys. Rev. B* **36**, 536 (1987).
- [4] T. Vojta, Smearing of the phase transition in Ising systems with planar defects, *J. Phys. A: Math. Gen.* **36**, 10921 (2003).
- [5] A. J. Bray and M. A. Moore, On the eigenvalue spectrum of the susceptibility matrix for random spin systems, *J. Phys. C: Solid State Phys.* **15**, L765 (1982).
- [6] M. Radeira, J. P. Sethna, and R. G. Palmer, Low-frequency relaxation in Ising spin-glasses, *Phys. Rev. Lett.* **54**, 1321 (1985).
- [7] A. H. Castro Neto, G. Castilla, and B. A. Jones, Non-Fermi liquid behavior and Griffiths phase in  $f$ -electron compounds, *Phys. Rev. Lett.* **81**, 3531 (1998).
- [8] M. C. De Andrade, R. Chau, R. P. Dickey, N. R. Dilley, E. J. Freeman, D. A. Gajewski, M. B. Maple, R. Movshovich, A. H. Castro Neto, G. Castilla, and B. A. Jones, Evidence for a common physical description of non-Fermi-liquid behavior in chemically substituted  $f$ -electron systems, *Phys. Rev. Lett.* **81**, 5620 (1998).
- [9] A. M. Pereira, L. Morellon, C. Magen, J. Ventura, P. A. Algarabel, M. R. Ibarra, J. B. Sousa, and J. P. Araújo, Griffiths-like phase of magnetocaloric  $R_5(\text{Si}_x\text{Ge}_{1-x})_4$  ( $R = \text{Gd}, \text{Tb}, \text{Dy}$ , and  $\text{Ho}$ ), *Phys. Rev. B* **82**, 172406 (2010).
- [10] N. Marcano, P. A. Algarabe, L. Fernández Barquín, J. P. Araújo, A. M. Pereira, J. H. Belo, C. Magén, L. Morellón, and M. R. Ibarra, Cluster-glass dynamics of the Griffiths phase in  $\text{Tb}_5\text{La}_{5-x}\text{Si}_2\text{Ge}_2$ , *Phys. Rev. B* **99**, 054419 (2019).
- [11] M. B. Salamon, P. Lin, and S. H. Chun, Colossal magnetoresistance is a Griffiths singularity, *Phys. Rev. Lett.* **88**, 197203 (2002).
- [12] J. Burgy, M. Mayr, V. Martin-Mayor, A. Moreo, and E. Dagotto, Colossal effects in transition metal oxides caused by intrinsic inhomogeneities, *Phys. Rev. Lett.* **87**, 277202 (2001).
- [13] D. Bhoi, N. Khan, A. Midya, M. Nandi, A. Hassen, P. Choudhury, and P. Mandal, Formation of nanosize Griffiths-like clusters in solid solution of ferromagnetic manganite and cobaltite, *J. Phys. Chem. C* **117**, 16658 (2013).
- [14] C. Magen, P. A. Algarabel, L. Morellon, M. R. Ibarra, A. M. Pereira, and J. B. Sousa, Observation of a Griffiths-like phase in the magnetocaloric compound  $\text{Tb}_5\text{Si}_2\text{Ge}_2$ , *Phys. Rev. Lett.* **96**, 167201 (2006).
- [15] J. Deisenhofer, D. Braak, H.-A. Krug von Nidda, J. Hemberger, R. M. Eremina, V. A. Ivanshin, A. M. Balbashov, G. Jug, A. Loidl, T. Kimura, and Y. Tokur, Observation of a Griffiths phase in paramagnetic  $\text{La}_{1-x}\text{Sr}_x\text{MnO}_3$ , *Phys. Rev. Lett.* **95**, 257202 (2005).
- [16] A. Ślebarski, J. Goraus, and M. Fijałkowski, Short-range ferromagnetic correlations in disordered  $\text{FeVGa}$  with distinct similarities to the Griffiths phase, *Phys. Rev. B* **84**, 075154 (2011).
- [17] A. K. Patel, S. S. Samatham, A. V. Lukoyanov, P. D. Babuf, and K. G. Suresh, Nearly compensated ferrimagnetic behaviour and giant exchange bias of hexagonal  $\text{Mn}_2\text{PtAl}$ : Experimental and theoretical studies, *Phys. Chem. Chem. Phys.* **24**, 29539 (2022).
- [18] J. Nag, P. C. Sreeparvathy, R. Venkatesh, P. D. Babu, K. G. Suresh, and A. Alam, Nontrivial topological features and Griffiths-phase behavior in  $\text{CrFeVGa}$  probed by experiment and theory, *Phys. Rev. Appl.* **19**, 044071 (2023).
- [19] T. J. Burch, T. Litrenta, and J. I. Budnick, Hyperfine studies of site occupation in ternary systems, *Phys. Rev. Lett.* **33**, 421 (1974).
- [20] J. Barth, B. Balke, G. H. Fecher, H. Stryhanyuk, A. Gloskovskii, S. Naghavi, and C. Felser, Thermoelectric properties of  $\text{CoTiSb}$  based compounds, *J. Phys. D: Appl. Phys.* **42**, 185401 (2009).
- [21] G. J. Li, E. K. Liu, H. G. Zhang, J. F. Qian, H. W. Zhang, J. L. Chen, W. H. Wang, and G. H. Wu, Unusual lattice constant changes and tunable magnetic moment compensation in  $\text{Mn}_{50-x}\text{Co}_{25}\text{Ga}_{25+x}$  alloys, *Appl. Phys. Lett.* **101**, 102402 (2012).

- [22] S. Roy, E. Blackburn, S. M. Valvidares, M. R. Fitzsimmons, S. C. Vogel, M. Khan, I. Dubenko, S. Stadler, N. Ali, S. K. Sinha, and J. B. Kortright, Delocalization and hybridization enhance the magnetocaloric effect in Cu-doped  $\text{Ni}_2\text{MnGa}$ , *Phys. Rev. B* **79**, 235127 (2009).
- [23] T. Gottschall, A. Grácia-Condal, M. Fries, A. Taubel, L. Pfeuffer, L. Mañosa, A. Planes, K. P. Skokov, and O. Gutfleisch, A multicaloric cooling cycle that exploits thermal hysteresis, *Nat. Mater.* **17**, 929 (2018).
- [24] Z. Li, Z. Li, D. Li, J. Yang, B. Yang, Y. Hu, D. Wang, Y. Zhang, C. Esling, X. Zhao, and L. Zuo, Achieving a broad refrigeration temperature region through the combination of successive caloric effects in a multiferroic  $\text{Ni}_{50}\text{Mn}_{35}\text{In}_{15}$  alloy, *Acta Mater.* **192**, 52 (2020).
- [25] R. Kainuma, Y. Imano, W. Ito, Y. Sutou, H. Morito, S. Okamoto, O. Kitakami, K. Oikawa, A. Fujita, T. Kanomota, and K. Ishida, Magnetic-field-induced shape recovery by reverse phase transformation, *Nature (London)* **439**, 957 (2006).
- [26] V. A. Lvov, S. Kustov, and E. Cesari, Enhancement of deformation of Ni–Mn–Ga martensite by dynamic loading, *Acta Mater.* **56**, 802 (2008).
- [27] F. Tian, Q. Zhao, J. Guo, S. Kong, B. Liu, Z. Dai, M. Fang, Y. Zhang, C. Zhou, K. Cao, and S. Yang, A giant exchange bias effect due to enhanced ferromagnetism using a mixed martensitic phase in  $\text{Ni}_{50}\text{Mn}_{37}\text{Ga}_{13}$  spun ribbons, *Nanomaterials* **13**, 2827 (2023).
- [28] B. M. Wang, Y. Liu, P. Ren, B. Xia, K. B. Ruan, J. B. Yi, J. Ding, X. G. Li, and L. Wang, Large exchange bias after zero-field cooling from an unmagnetized state, *Phys. Rev. Lett.* **106**, 077203 (2011).
- [29] J. Jeong, Y. Ferrante, S. V. Faleev, M. G. Samant, C. Felser, and S. S. P. Parkin, Termination layer compensated tunnelling magnetoresistance in ferrimagnetic Heusler compounds with high perpendicular magnetic anisotropy, *Nat. Commun.* **7**, 10276 (2016).
- [30] S. V. Faleev, Y. Ferrante, J. Jeong, M. G. Samant, B. Jones, and S. S. P. Parkin, Heusler compounds with perpendicular magnetic anisotropy and large tunneling magnetoresistance, *Phys. Rev. Mater.* **1**, 024402 (2017).
- [31] H. Ishikawa, R. Y. Umetsu, K. Kobayashi, A. Fujita, R. Kainuma, and K. Ishida, Atomic ordering and magnetic properties in  $\text{Ni}_2\text{Mn}(\text{Ga}_x\text{Al}_{1-x})$  Heusler alloys, *Acta Mater.* **56**, 4789 (2008).
- [32] R. Nevgi, E. T. Dias, and K. R. Priolkar, Randomly packed  $\text{Ni}_2\text{MnIn}$  and  $\text{NiMn}$  structural units in off-stoichiometric  $\text{Ni}_2\text{Mn}_{2-y}\text{In}_y$  alloys, *Phys. Rev. B* **104**, 054101 (2021).
- [33] J. Valenta, M. Kratochvílová, M. Míšek, K. Carva, J. Kaštil, P. Doležal, P. Opletal, P. Cermák, P. Proschek, K. Uhlířová, J. Prchal, M. J. Coak, S. Son, J-G. Park, and V. Sechovský, Pressure-induced large increase of Curie temperature of the van der Waals ferromagnet  $\text{VI}_3$ , *Phys. Rev. B* **103**, 054424 (2021).
- [34] F. Mende, J. Noky, S. N. Guin, G. H. Fecher, K. Manna, P. Adler, W. Schnelle, Y. Sun, C. Fu, and C. Felser, Large anomalous Hall and Nernst effects in high Curie-temperature iron-based Heusler compounds, *Adv. Sci.* **8**, 2100782 (2021).
- [35] J. Mao, Y. Sui, X. Zhang, Y. Su, X. Wang, Z. Liu, Y. Wang, R. Zhu, Y. Wang, W. Liu, and J. Tang, Temperature- and magnetic-field-induced magnetization reversal in perovskite  $\text{YFe}_{0.5}\text{Cr}_{0.5}\text{O}_3$ , *Appl. Phys. Lett.* **98**, 192510 (2011).
- [36] H. W. F. Sung and C. Rudowicz, Physics behind the magnetic hysteresis loop—A survey of misconceptions in magnetism literature, *J. Magn. Magn. Mater.* **260**, 250 (2003).
- [37] E. Oumezzine, M. Oumezzine, and E. K. Hlil, Landau mean-field analysis of magnetic entropy change and determination of spontaneous magnetization in  $\text{La}_{0.6}\text{Pr}_{0.1}\text{Ba}_{0.3}\text{MnO}_3$  perovskite, *J. Alloy Compd.* **682**, 366 (2016).
- [38] F. Tian, Y. Zeng, M. Xu, S. Yang, T. Lu, J. Wang, T. Chang, M. Adil, Y. Zhang, C. Zhou, and X. Song, A magnetocaloric effect arising from a ferromagnetic transition in the martensitic state in Heusler alloy of  $\text{Ni}_{50}\text{Mn}_{36}\text{Sb}_8\text{Ga}_6$ , *Appl. Phys. Lett.* **107**, 012406 (2015).
- [39] L. Zhou, M. M. Schneider, A. Giri, K. Cho, and Y. Sohn, Microstructural and crystallographic characteristics of modulated martensite, non-modulated martensite, and pre-martensitic tweed austenite in Ni–Mn–Ga alloys, *Acta Mater.* **134**, 93 (2017).
- [40] H. R. Zhang and G. H. Wu, Atomic-size effect on the microstructural properties of  $\text{Ni}_2\text{FeGa}$ , *Acta Mater.* **59**, 1249 (2011).
- [41] D. Liu, J. Gou, Z. Xu, Y. Liu, and T. Ma, Atomic scale understanding the periodic modulation in ferroelastic alloy Ni–Mn–Ti, *Acta Mater.* **248**, 118768 (2023).
- [42] J. S. Zhou and J. B. Goodenough, Local structural distortions, orbital ordering, and ferromagnetism in underdoped  $\text{La}_{1-x}\text{Sr}_x\text{MnO}_3$ , *Phys. Rev. B* **91**, 064414 (2015).
- [43] L. Zhang, J. Li, Y. Du, J. Wang, X. Wei, J. Zhou, J. Cheng, W. Chu, Z. Jiang, Y. Huang, C. Yan, S. Zhang, and Z. Wu, Lattice distortion and its role in the magnetic behavior of the Mn-doped ZnO system, *New J. Phys.* **14**, 013033 (2012).
- [44] F. Tian, X. Ke, K. Cao, D. Wang, Q. Zhao, J. Li, Z. Dai, D. Wang, Y. Zhang, C. Zhou, Y. Wang, W. Zuo, M. Fang, and S. Yang, Tailoring exchange bias in reentrant spin glass by ferromagnetic cluster size engineering, *APL Mater.* **9**, 011104 (2021).
- [45] S. Gupta, S. Chakraborty, S. Pakhira, A. Biswas, Y. Mudryk, A. Kumar, B. Mukherjee, G. S. Okram, A. Das, V. K. Pecharsky, and C. Mazumdar, Experimental observation of spin glass state in the highly disordered quaternary Heusler alloy  $\text{FeRuMnGa}$ , *Phys. Rev. B* **107**, 184408 (2023).
- [46] P. Bag, P. R. Baral, and R. Nath, Cluster spin-glass behavior and memory effect in  $\text{Cr}_{0.5}\text{Fe}_{0.5}\text{Ga}$ , *Phys. Rev. B* **98**, 144436 (2018).
- [47] S. Pakhira, C. Mazumdar, R. Ranganathan, S. Giri, and M. Avdeev, Large magnetic cooling power involving frustrated antiferromagnetic spin-glass state in  $R_2\text{NiSi}_3$  ( $R = \text{Gd}, \text{Er}$ ), *Phys. Rev. B* **94**, 104414 (2016).
- [48] M. Saslow and G. Parker, “Melting” of frustrated spins: Mechanism for reentrant ferromagnetic-spin-glass behavior, *Phys. Rev. Lett.* **56**, 1074 (1986).
- [49] K. Binder and A. P. Young, Spin glasses: Experimental facts, theoretical concepts, and open questions, *Rev. Mod. Phys.* **58**, 801 (1986).
- [50] J. L. Victor, M. Gaudon, G. Salvatori, O. Toulemonde, N. Penin, and A. Rougier, Doubling of the phase transition temperature of  $\text{VO}_2$  by Fe doping, *J. Phys. Chem. Lett.* **12**, 7792 (2021).